

Ablation Path Saliency

Justus Sagemüller

Olivier Verdier

September 27, 2022

Various types of saliency methods have been proposed for explaining black-box classification. In image applications, this means highlighting the part of the image that is most relevant for the current decision.

We observe that several of these methods can be seen as edge cases of a single, more general procedure based on finding a particular *ablation path* through the classifier’s domain. This gives additional geometric insight to the existing methods.

We also demonstrate that this ablation path method can be used as a technique in its own right, the higher computational cost being traded against additional information given by the path.

1. Introduction

The basic idea of *saliency* or *attribution* is to provide insights as to why a neural network produces a given output (for instance, a classification) for a given input (for instance, an image). There is no clear consensus in the literature as to what saliency should exactly be, but various properties that such a method should fulfill have been proposed. All the methods discussed here start out by contrasting the given input (also called *current target*) with another one, called *baseline*, which should be neutral in at least the sense of not displaying any of what causes the target image’s classification. The saliency problem then amounts to finding out what the features of the target are which cause it to be classified differently from the baseline.

In [13] the authors give axioms attempting to make it precise what that means. Of these, *sensitivity* captures most of the notion of saliency, namely, that the features on which the output is most sensitive should be given a higher saliency value. The authors give further axioms to narrow it down: implementation invariance, completeness, linearity and symmetry preservation. They obtain a corresponding method: the Integrated Gradient method. Despite the attempt to thus narrow down the choice of saliency method, Integrated Gradient has not established itself as a default in the community. Indeed the axioms used to justify it are not altogether self-evident.

In [4], a method is provided whose construction is quite different. Instead of following axioms about the properties a method should have, they produce a result that has direct

2. Related Work

meaning associated to it, namely as a mask that preserves only certain parts of the input and removes others, optimised so that the classification is retained even at high degrees of ablation, i.e., when the mask only keeps small part of the target image. This method is highly appealing, but in practice the optimisation problem is ill-conditioned and can only be solved under help of regularization techniques. That prevents this technique, too, from being a definite saliency method or “the” saliency method.

Various other methods from the literature are in a broadly similar position, all with certain arguments for their use but also various practical limitations and no clear reason to favour them over the alternatives. In some cases there are evident mathematical relationships between the methods, but they have not been investigated thoroughly yet or exploited for a unifying generalization.

This is what our paper provides: it introduces *ablation paths*, which take up and extend the idea of integrating from the baseline to the target image. It combines this with the notion of ablation / masks, in that each step along the path can constitute a mask highlighting progressively smaller portions of the image. The main purpose of this is mathematical unification and better (meta-) understanding of the various methods, but ours can also be used as a saliency method by itself.

A summary how the method works: suppose first that images are defined over a domain Ω , which can be regarded as the set of pixels in the discrete case, or as a domain such as a square, for the image at infinite resolution. We define *ablation paths* as parameter dependent smooth masks $\varphi: [0, 1] \rightarrow \mathcal{C}(\Omega, \mathbb{R})$, with the further requirement that the mask at zero, $\varphi(0)$, should be zero over the domain Ω , and the mask at one, $\varphi(1)$, should be one over the domain Ω . We also impose that, at each pixel, the mask value increases over time (see Figure 1), and that this happens with a constant area speed: the area covered by the mask should increase linearly over time (see § 3). Let F be the classifier, which outputs a probability between zero and one. We choose a current image of interest x_0 and a *baseline image* x_1 . The objective function P is then $P(\varphi) := \int_0^1 F(x_0 + \varphi(t)(x_1 - x_0)) dt$ (see § 4). Assuming that $F(x_0) \simeq 1$ and $F(x_1) \simeq 0$, maximising the objective function means that we try to find an ablation path that stays as long as possible in the decision region of x_0 . Intuitively, we try to replace as many pixels of x_0 by pixels of x_1 while staying in the same class as x_0 .

2. Related Work

[11] defines a saliency map as the gradient of the network output at the given image. This would appear to be a sensible definition, but the resulting saliency is very noisy because the network output is roughly constant around any particular image. [10] improves the situation by computing the gradient after each layer instead. This is, however, not a black-box method such as the one we propose. [7] computes an *influence function*, that is, a function that measures how the parameters would be changed by a change in the training data. Although it is a black-box method, it is not a saliency method per se. They use the gradient of the network output to find the pixel most likely to have a high saliency. The pixels that have most effect are given a higher saliency.

2. Related Work

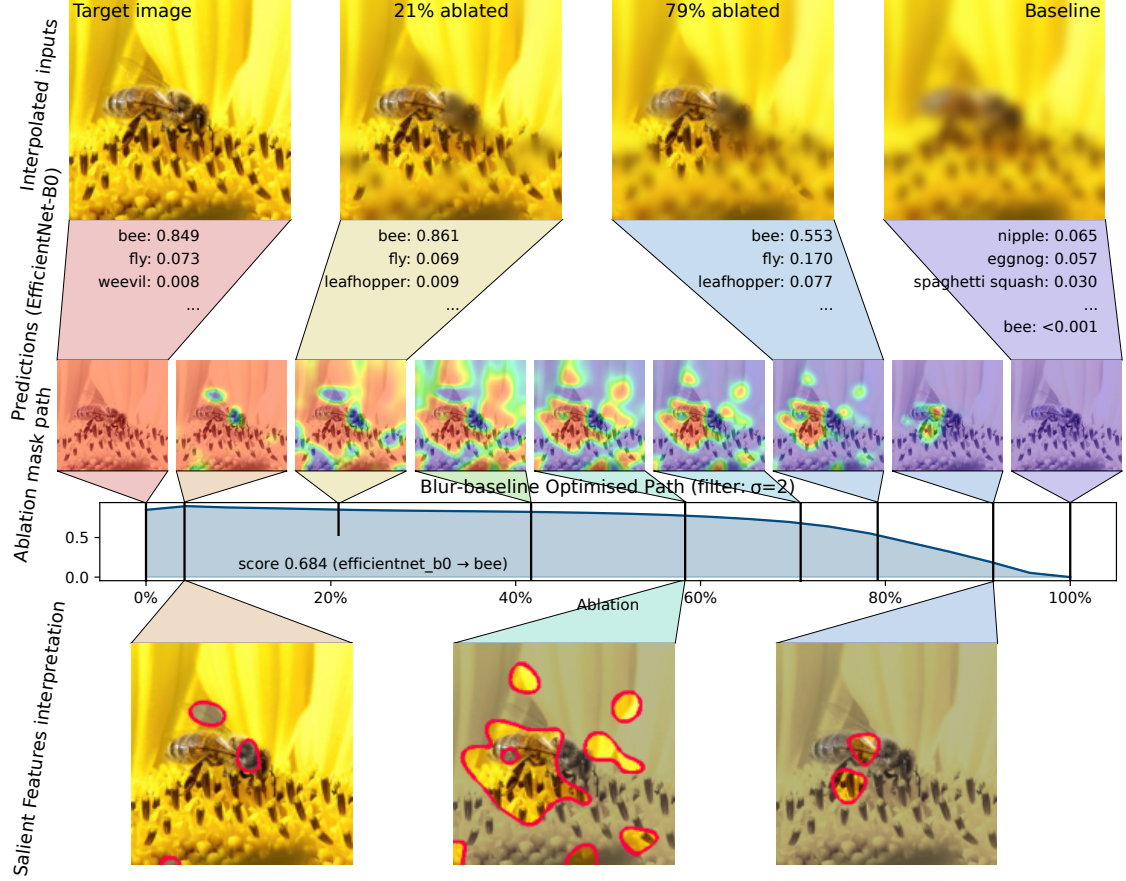


Figure 1.: Example of how an ablation path (sequence of masks, middle row) gives rise to a transition between a current target (a bee from ImageNet) and a baseline (blurred version of the same image). See § 6 for discussion of this example.

By contrast, [8] proposes to directly evaluate the saliency by finding out which pixels most affect the output, similarly to [4], but without using any gradients. These methods can be seen as different ways of solving similar optimisation problems, the solution of which produces a mask (cf. § 3.1) highlighting features of importance.

There are also a number of meta-studies of saliency methods. [1] lists essential properties, for instance the requirement that the results should depend on the training data in a sense that perturbing *model parameters* should change the saliency. [6] proposes a number of property that saliency methods should satisfy. [2] compares several saliency methods and proposes a method to evaluate them (the sensitivity- n property).

These properties were not in the main focus of the design of our method, however we do fulfill the general criteria. For example, [6] is concerned with constant shifts in the inputs. If such a shift is applied to both the target and baseline, then the modification commutes through the interpolation and if we then assume a modified network that deals with such inputs in the same way as the original did with unshifted ones then all

3. Ablation Paths

the gradients will be the same, therefore the optimised paths will also be the same.

3. Ablation Paths

3.1. Images and Masks

We assume data represented on a compact domain Ω . In case of an image made of pixels, this would be a discretised rectangle, so $\Omega = \{1, \dots, n\} \times \{1, \dots, m\}$, but note that it could as well be continuous, in which case, $\Omega = [0, a] \times [0, b]$. What matters to us is that Ω is equipped with a positive measure. In the following, \int_{Ω} denotes integration with respect to that measure. Without loss of generality, we assume the mass of that measure to be one, i.e., $\int_{\Omega} 1 = 1$.

The data itself consists of functions on Ω with values in a vector space V (the dimensions of V may typically represent the *colour channels*). We call the space of these functions/images \mathcal{I} . It can be seen as a *module* equipped with a commutative ring \mathcal{M} , which represents *masks*. Concretely, in most of the paper we choose

$$\mathcal{I} := \mathcal{C}(\Omega, V) \quad \mathcal{M} := \mathcal{C}(\Omega, \mathbb{R}).$$

The module structure simply describes that masks can multiply images, i.e., that the operation θx gives a new image in \mathcal{I} when $\theta \in \mathcal{M}$ and $x \in \mathcal{I}$, and that this operation is bilinear.

3.2. Ablation Paths

Definition 3.1. We define the set \mathcal{A} of *ablation paths* as the set of functions $\varphi: [0, 1] \rightarrow \mathcal{M}$ fulfilling the following properties:

Boundary conditions $\varphi(0) = 0$ and $\varphi(1) = 1$

Monotonicity $t_1 \leq t_2 \implies \varphi(t_1) \leq \varphi(t_2) \quad t_1, t_2 \in [0, 1]$

Constant speed $\int_{\Omega} \varphi(t) = t \quad t \in [0, 1]$.

We will call *monotone paths* the paths that fulfill the first two conditions but not the third.

Note that the set \mathcal{A} of ablation paths is a *convex subset* inside the set of possible paths denoted by $\mathcal{P} := \mathcal{L}^{\infty}([0, 1], \mathcal{M})$.

Some comments on each of those requirements are in order. (i) 0 and 1 denote here the constant functions zero and one (which corresponds to the zero and one of the algebra \mathcal{M}) (ii) $\varphi(t_1) \leq \varphi(t_2)$ should be interpreted as usual as $\varphi(t_2) - \varphi(t_1)$ being in the cone of nonnegative elements¹. (iii) If $t \mapsto \int_{\Omega} \varphi(t)$ is differentiable, this requirement can be rewritten as $\frac{d}{dt} \int_{\Omega} \varphi(t) = 1$, so it can be regarded as a *constant speed* requirement.

¹Here we can define the cone of nonnegative functions by $\{f \in \mathcal{C}(\Omega, \mathbb{R}) \mid f \geq 0\}$. In a general star algebra, this cone would be defined as $\{x \in R \mid \exists y \in R \quad x = y^*y\}$.

3. Ablation Paths

This requirement is more a normalisation than a requirement, as is further detailed in Remark 3.4.

The simplest (requirement-fulfilling) ablation path is the *affine interpolation path*:

$$\ell(t) := t. \quad (1)$$

The mask is thus constant in space at each time t . This path is implicitly used in [13]: its image-application corresponds to affine interpolation between target- and baseline image.

Note that an ablation path without the constant-speed property can always be transformed into one that does fulfil it. This is clear if the function $t \mapsto \int_{\Omega} \varphi(t)$ is strictly increasing, as this is then just a time reparameterisation, but this is in fact always possible, in a canonical sense. The proof is in Appendix A.

Lemma 3.2. *To any monotone path there corresponds a canonical ablation path.*

Remark 3.3. Since \mathcal{M} is a function space, an ablation path φ is a function of one argument, but its value is itself a function, so φ can also be regarded as a function of *two* arguments instead. In the sequel, we will therefore abuse the notations and write φ as a function of one or two arguments depending on the context, that is, we will identify $\varphi(t) \equiv \varphi(t, \cdot)$. For instance, in the definition Definition 3.1 above, $\int_{\Omega} \varphi(t) \equiv \int_{\Omega} \varphi(t, \cdot) \equiv \int_{\Omega} \varphi(t, \mathbf{r}) \, d\mathbf{r}$.

Remark 3.4. If the ablation path φ is differentiable in time, the requirements in Definition 3.1 admit a remarkable reformulation. Define $\psi(t) := \frac{d}{dt} \varphi(t)$. All the requirements in Definition 3.1 are equivalent to the following requirements for a function $\psi: [0, 1] \times \Omega \rightarrow \mathbb{R}$:

$$\psi(t, \mathbf{r}) \geq 0, \quad \int_{\Omega} \psi(t, \mathbf{r}) \, d\mathbf{r} = 1, \quad \int_{[0,1]} \psi(t, \mathbf{r}) \, dt = 1 \quad t \in [0, 1], \mathbf{r} \in \Omega$$

The corresponding ablation path φ is then recovered by $\varphi(t) := \int_0^t \psi(s) \, ds$. What this means is that differentiable ablation paths can be parameterised as densities of *doubly stochastic Markov transition kernels* on $[0, 1] \times \Omega$.

3.3. Regularity of Ablation Paths

Even with the constraints on what paths constitute valid ablation, the set of these paths cannot be expected to consist of particularly regular functions, neither in space nor time. However, at least the following weak sense of regularity is automatically guaranteed:

Lemma 3.5. *If φ is an ablation path, then*

$$\|\varphi(t_1) - \varphi(t_0)\|_{\mathcal{L}^1} = |t_1 - t_0|.$$

In particular, $t \mapsto \varphi(t, \cdot)$ is continuous as a function $[0, 1] \rightarrow \mathcal{L}^1(\Omega)$.

Proof. Choose t_0, t_1 in $[0, 1]$. Without loss of generality, assume $t_1 \geq t_0$. Then, $\int_{\Omega} |\varphi(t_1) - \varphi(t_0)| = \int_{\Omega} (\varphi(t_1) - \varphi(t_0)) = t_1 - t_0$, from which we conclude that $\varphi(t_1) - \varphi(t_0)$ is in \mathcal{L}^1 and fulfils the equation above. \square

4. Score of an Ablation Path

Ultimately, the saliency method aims at providing insights about the classification of the given input $x_0 \in \mathcal{I}$, and should therefore only depend on that image. We will however also use a so-called *baseline image*, denoted by $x_1 \in \mathcal{I}$, which may be a different real-world sample or some neutral input (see e.g. [12] for a discussion of various possibilities).

We propose the following measure of the *score* of an ablation path (in the sense of Definition 3.1) with respect to these two images. Given a *mask* $\theta \in \mathcal{M}$, we write the *interpolated image* $[x_0, x_1]_\theta \in \mathcal{I}$ as

$$[x_0, x_1]_\theta := (1 - \theta)x_0 + \theta x_1 \quad \theta \in \mathcal{M}, \quad x_0, x_1 \in \mathcal{I}.$$

Note that if $\theta = 0$, that is, the mask θ is identitically zero, then $[x_0, x_1]_0 = x_0$, and if $\theta = 1$, that is, the mask θ is identically one, then $[x_0, x_1]_1 = x_1$. This leads us to use the shorthand notation:

$$x_\theta := [x_0, x_1]_\theta \quad \theta \in \mathcal{M} \quad (x_0, x_1 \in \mathcal{I}).$$

We now define the *score function* $P: \mathcal{P} \rightarrow \mathbb{R}$ from paths to real numbers by the integral

$$P(\varphi) := \int_0^1 F(x_{\varphi(t)}) dt. \quad (2)$$

Note that, as F is bounded between zero and one, so is $P(\varphi)$ for any ablation path $\varphi \in \mathcal{A}$. The main idea is that if $F(x_0) \simeq 1$ and $F(x_1) \simeq 0$, so the higher this value of P is, the better the path is to describe the salient parts of the image.

It is straightforward to compute its differential dP on the space of paths \mathcal{P} :

$$\langle dP, \delta\varphi \rangle = \int_0^1 \underbrace{\langle dF_{x_{\varphi(t)}}, \rangle}_{\in \mathcal{I}^*} \underbrace{(x_1 - x_0)}_{\in \mathcal{I}} \underbrace{\delta\varphi(t)}_{\in \mathcal{M}} dt \quad \delta\varphi \in \mathcal{P}.$$

So if we define the product of $D \in \mathcal{I}^*$ and $x \in \mathcal{I}$ producing an element in \mathcal{M}^* by $\langle xD, \varphi \rangle := \langle D, x\varphi \rangle$ as is customary², we can rewrite this differential as

$$\langle dP, \delta\varphi \rangle = \int_0^1 \langle (x_1 - x_0) dF_{x_{\varphi(t)}}, \delta\varphi(t) \rangle dt.$$

Note that we know that any ablation path is bounded, so $\varphi \in \mathcal{L}^\infty([0, 1], \mathcal{M})$, so the differential of P at φ can be identified with the function $dP_\varphi = [t \mapsto (x_1 - x_0) dF_{x_{\varphi(t)}}]$ in $\mathcal{L}^1([0, 1], \mathcal{M}^*)$.

4.1. Relation with the Integrated Gradient Method

When this differential is computed on the interpolation path ℓ (1) and then *averaged*, then this is exactly the integrated average gradient [13]. More precisely, the integrated gradient is exactly $\int_0^1 dP_{\ell(t)} dt$. Note that this is in fact an integrated *differential*, since we obtain an element in the dual space \mathcal{I}^* , and this differential should be appropriately smoothed along the lines of § 5.1.

²For instance in the theory of distributions.

5. Optimisation Problem and Algorithm

4.2. Relation to Pixel Ablation

Given any saliency function $\sigma \in \mathcal{M}$ (for example an integrated gradient, meaningful-perturbation, or grad-CAM result) we can define a path by

$$\tilde{\varphi}(t) := \mathbf{1}_{\sigma \leq \log(t/(1-t))} \text{ when } t \in (0, 1) \quad (3)$$

and $\tilde{\varphi}(0) := 0$, $\tilde{\varphi}(1) := 1$. This path is a monotone path, except in the module of images $\mathcal{I} = \mathcal{L}^2(\Omega, V)$, equipped with the ring of masks $\mathcal{M} = \mathcal{L}^\infty(\Omega)$. To be an ablation path, it still needs to be transformed into a constant speed path, which is always possible as explained in Appendix A.

That results in a generalisation of the pixel-ablation scores used in [8] and [12]. In that case, the set Ω would be a discrete set of pixels, which are being sequentially switched from “on” to “off” by the (binary) mask.

Note that in the ranking, pixels with the same saliency would be ranked in an arbitrary way and added to the mask in that arbitrary order. In the method of Equation 3, we add such pixels all at once, which seems preferable because it does not incur an arbitrary bias between pixels. The time reparameterisation keeps the function constant longer to account for however *many* pixels were ranked the same. As long as the ranking is strict (no two pixels have the same saliency), the method is the same as discrete pixel ranking.

4.3. Relation to Meaningful Perturbations

In the saturated case, that is, if F only takes values zero and one (or in the limit where it does), our method reduces to finding the interpolation with the largest mask on the boundary, equivalent to the approach of [4]. This is a result of the following: suppose that the ablation path φ crosses the boundary at time t^* . It means that $F(x_{\varphi(t)})$ has value one until t^* and zero afterwards, so the score P defined in (2) is $P(\varphi) = t^*$. By the constant speed property, $t^* = \int_{\Omega} \varphi(t^*)$, so we end up maximising the mask area on the boundary.

5. Optimisation Problem and Algorithm

We proceed to define the optimisation problem that we propose as a saliency method, and how to solve it numerically.

Conceptually we try to find the ablation path (see Definition 3.1) that maximises the score $P(\varphi)$:

$$\max_{\varphi \in \mathcal{A}} P(\varphi).$$

Recall that the set \mathcal{A} of ablation paths is convex; however, since the objective function P is not convex, this is not a convex optimisation problem.

The method we suggest is to follow a gradient direction. Such an approach is in general not guaranteed to approximate a global maximum, a common problem with many practical applications. However, empirical results (see § 6) suggests that gradient descent does often manage to approximate global maxima, particularly obvious in the unregularised near-perfect scores.

6. Examples

5.1. Gradient and Metric

We suggest to use a gradient descent algorithm. However, in order to do this, we need to be able to compute gradients (this is sometimes called “natural gradients” in the literature). Differentiating a real-valued function defined on the space \mathcal{P} gives a *differential*, which is an element of the dual space \mathcal{P}^* . In the Euclidean case that space is canonically isomorphic to \mathcal{P} , thus the common practice to use it directly as a *gradient* in \mathcal{P} , which is usable as contribution to a state update. But in general, this requires first a map from that space to \mathcal{P} , and even in a discretised realisation it is prudent to consider this map explicitly, since the implied one depends on the (pixel) basis choice. For now we assume that $\varphi \in \mathcal{L}^2([0, 1], \mathcal{M})$ and $dP \in \mathcal{L}^2([0, 1], \mathcal{M}^*)$.

However, we still need a mapping $K: \mathcal{M}^* \rightarrow \mathcal{M}$. In practice, a reasonable choice is the covariance operator associated to a smoothing operation. For a measure $\mu \in \mathcal{M}^*$, $\langle K\mu, \theta \rangle := \langle \mu, \int_{\Omega} k(\cdot - \mathbf{r})\theta(\mathbf{r}) d\mathbf{r} \rangle$, where k is a suitable smoothing function, for instance $k(\mathbf{r}) = \exp(-\|\mathbf{r}\|^2/\sigma)$. This provides us with a usable gradient of P .

Since the optimisation problem is *constrained* (the ablation path φ being constrained by the requirements in Definition 3.1), following the gradient direction will in general leave the set \mathcal{A} . Because the constraints are convex, it is straightforward enough to project each gradient-updated version back to something that does fulfill them, and indeed that is the idea behind our algorithm, however in practice it does by itself not yield convergence without impractically many iterations. See Appendix Appendix C for the details of how we actually proceed.

6. Examples

To test out our path-scoring approach and the saliency method based on its optimisation, we use standard image classifier deep-CNNs (Inception v4 [14] and EfficientNet [16], both pre-trained on ImageNet), with a selection of images from ILSVRC14 [9] for the current target. For the baseline we default to a blurred version of the target image, however it is in principle perfectly possible to use the method with other choices of baseline.

Our algorithm yields a whole path of masks, which cannot as a whole be visualised in one 2D view. This is different for previous saliency techniques, which produce a single heatmap. We find the additional information of the entire path substantially helpful for interpretability. For example, in Figure 1, note how the beginning of the path first *removes* the head and wing of the bee. This is counterintuitive, but a look at the classification reveals that those features are associated primarily with the `fly` class, and are therefore detrimental to a classification as `bee`, i.e., anti-salient features. The middle of the path then proceeds to remove irrelevant background features; the fact that the classification changes little in this segment and the masked regions are unsharp indicates that the exact locations have little relevance here. Finally, the masks again sharpen in to some parts of the bee itself, and only after these are removed the classification drops rapidly.

We call those last-highlighted regions the *threshold mask*, which we define as the mask right where the path crosses the decision boundary, and it is typically the most insightful

6. Examples

slice of the path: it still preserves enough of the image to be classified correctly, but no more. All of the images in this section refer to that selection, and where the threshold lies in the path is indicated by the vertical black line in the score plots. To be precise, this is the mask that preserves as little of the image as possible whilst still resulting in the intended class keeping the highest probability among the classes in the classifier’s prediction.

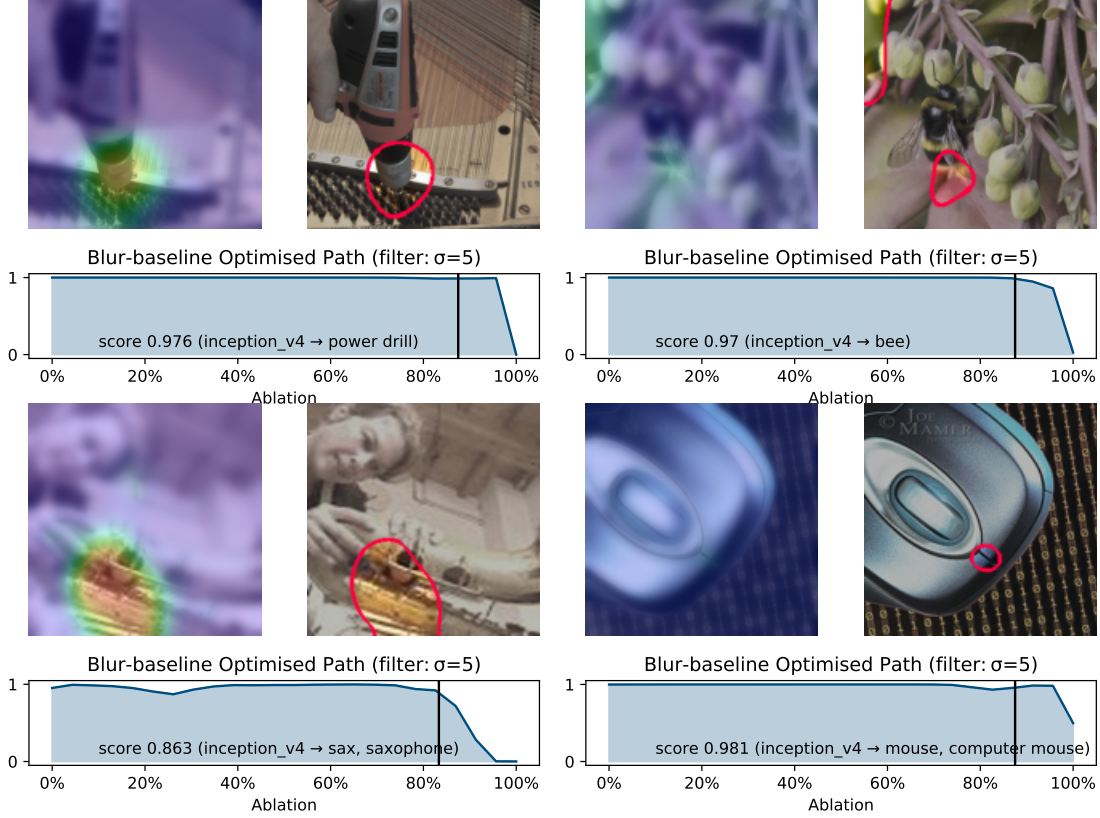


Figure 2.: Some examples of ablation path saliency for various images from ILSVRC14 [9].

Figure 2 displays various ways the threshold mask may look. In some cases it highlights very clearly features of the image that a human would consider a good reason, such as the chuck of the power drill or brass keys of the saxophone. In other cases it may highlight also unexpected e.g. background features, which may seem unsatisfying but is in fact testament to the method’s ability to highlight potentially problematic biases in a classifier.

While the method is designed to support highly saturated, near-boolean masks (which are particularly well interpretable), the optimisation does not always converge on such masks. In particular, notice how the examples on the right in Figure 2 are almost completely blurred in even the highly salient parts, and yet retain a high classification

6. Examples

of the original class. This seems to be essentially a vanishing-gradient problem, because the classifier (here Inception) behaves as a near-constant function. In principle, the path formulation is more robust to this issue because it is guaranteed to eventually cross the decision boundary, however this may not be sufficient if the crossing happens only after the last step in the discretised representation. See Appendix Appendix C for some discussion and on a strategy that can help to mitigate undersaturated masks.

Another issue is that optimising under only the constraints of § 3 allows for masks that are spatially very irregular. This way, very good path scores can be achieved, with sometimes a few individual pixels being enough to retain classification. This behaviour seems closely related to the known phenomenon of *adversarial examples* [15]. At any rate such results are hardly human-interpretable. The authors in [4] were confronted with similar problems. One explanation of this behaviour is that identifying the gradient with the differential implies that the space of masks \mathcal{M} is essentially bounded functions without further regularity (see § 5.1), similar to the mask space in § 4.2.

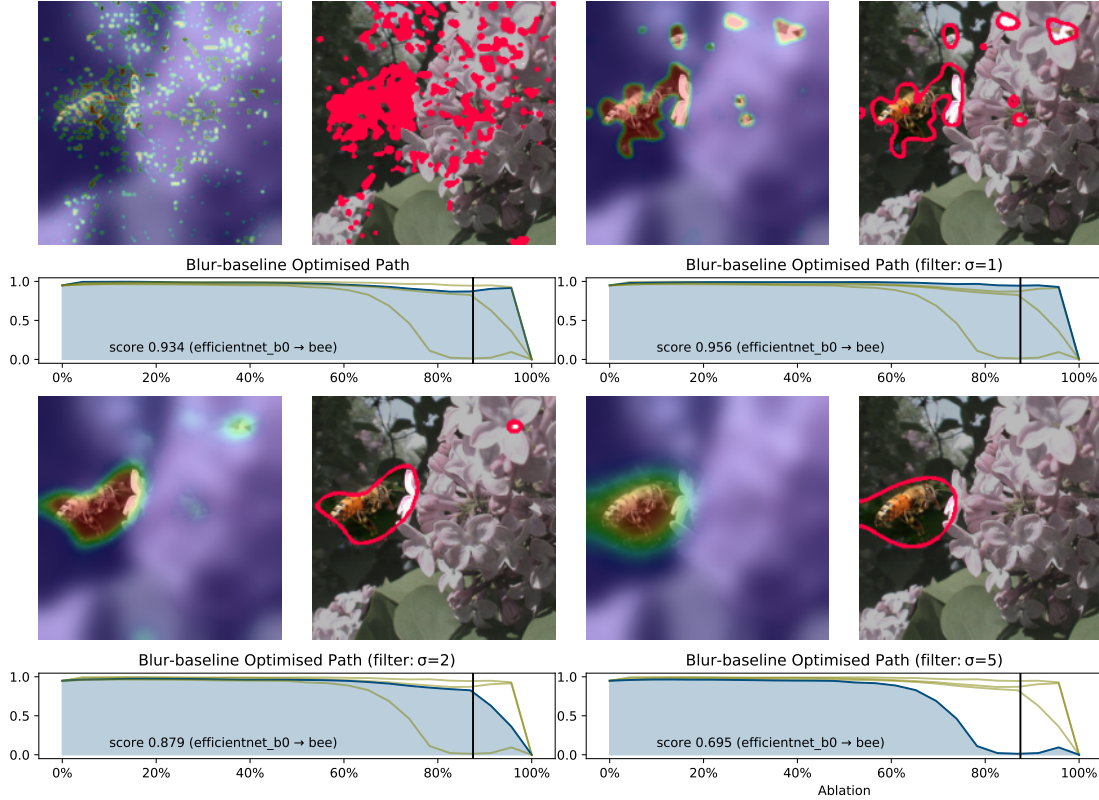


Figure 3.: Comparison of optimised ablation paths for an image of a bee against a blurred baseline, using different filtering parameters on the masks.

For the examples here, we used interspersed filtering in the optimisation procedure as a regularisation. The path-optimisation still typically manages to achieve high scores, but now highlights the eraser as a single, clearly interpretable feature. Note that a tradeoff

6. Examples

needs to be made (Figure 3); very small filtering can still result in highly disconnected masks, whereas too large-scale smoothing may prevent the algorithm from narrowing down on the features of interest.

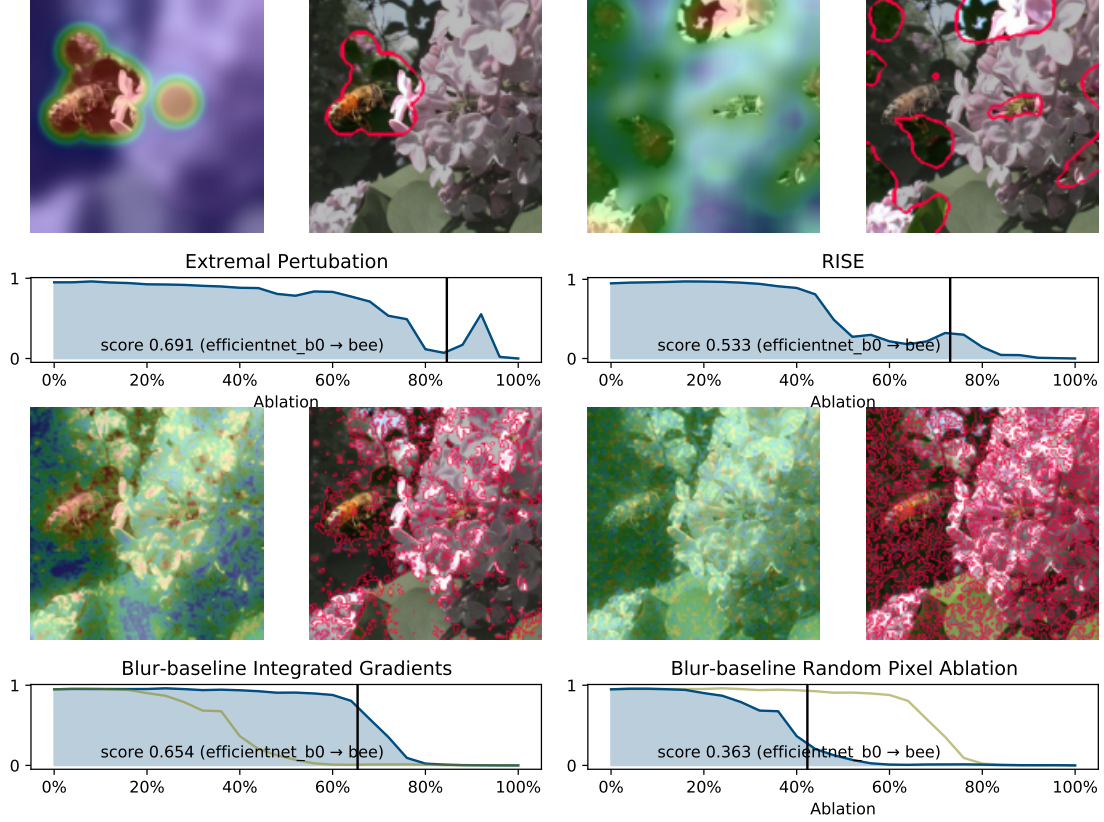


Figure 4.: The example from Figure 3 analysed with various methods from the literature. Extremal Perturbation [3] and RISE [8] as implemented in the TorchRay library [17] with default parameters. Integrated gradients as described in [13].

When comparing our results with single-mask saliency methods from the literature (Figure 4), the natural path-score to evaluate is the pixel ablation (cf. §4.2). It is known [8][12] that these methods generally achieve significantly better scores than random-order ablation of the pixels (cf. Appendix Appendix F), but our method usually achieves much higher scores yet. That is unsurprising, because it is specifically based on an optimisation of that score.

Practically speaking, saliency is particularly interesting in examples where it is unclear what the classification was based on or whether it is actually correct. In Figure 5, two images from the ImageNet **computer mouse** class are studied. The first one is by Inception initially classified as **keyboard** instead (notice the low mouse score at the left of the score graph); however optimising a path for **computer mouse** narrows down on the mouse itself, which is indeed classified as such. By contrast, EfficientNet classifies

7. Pointing game

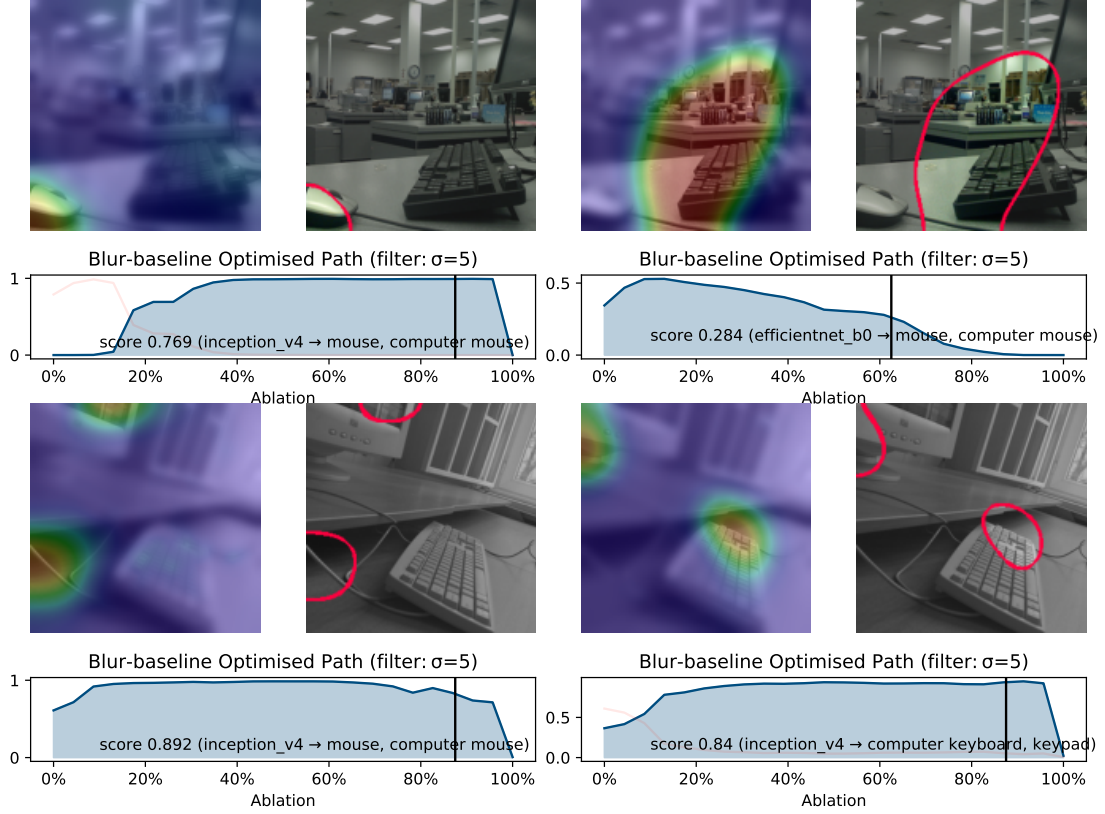


Figure 5.: Examples where the saliency method gives useful insights as to what objects in the image were actually responsible for the classification.

this image as a mouse from the start, but apparently bases its decision on background features instead.

In the second row of Figure 5, the mouse is not even in the selected frame of the image, yet ImageNet does classify this example as **computer mouse**. The optimised path reveals that this is based on the cables on the left and an edge of the screen. Meanwhile, optimising for **computer keyboard** instead focuses indeed on the keyboard, as well as another part of the screen.

There are more parameters that can affect the saliency outputs which we don't have space to present here, in particular the choice of baseline. See Appendix Appendix D for some more examples.

7. Pointing game

We evaluate our saliency algorithm using the pointing game method. This method was introduced in [19] and used, for instance, in [10][4]. Specifically, we check whether the maximum-salient pixel of the threshold mask lies within the bounding box of the object

7. Pointing game

Class (sample size)	Ablation path	Meaningful Perturbations
Bee (121)	83 %	46 %
Power drill (121)	77 %	40 %
Saxophone (119)	89 %	49 %

Table 1.: The success rate of the pointing game for various classes from the ILSVRC2014 dataset [9]. We chose the first images in each class by alphabetical order. We compare to the meaningful perturbation method in [4].

that defines the class.

Assessments like the pointing game of saliency methods clearly have their caveats. One can for instance argue that the cases when the saliency points somewhere outside the bounding box are the most insightful ones, as they indicate that the classifier is using information from an unexpected part of the image (for instance, the background). Another caveat is that, if winning at the pointing game is the goal, a saliency method is only as good as its underlying classifier is. We do *not* claim that the better score in Table 1 proves our method superior to the literature one. Anyway these results depend on the parameter choice (regularisation etc.). The meaningful-perturbation method could possibly achieve better scores, and ours would achieve worse with some parameter choice. The parameters that achieve best pointing-game score may not be the best for explainability purposes (in particular, the pointing game benefits from strong smoothing for stability, which may however remove interesting small-scale information).

Nevertheless, if a saliency method often hits the bounding box it is reasonable to conclude that both the classifier and the saliency method behave in an intuitive way, from a human perspective.

Our measurements confirm that the ablation-path method indeed does this well. Table 1 shows some results for our method on various images with blurred image as baseline. We show a few examples of this pointing game on Figure 6. See Appendix Appendix

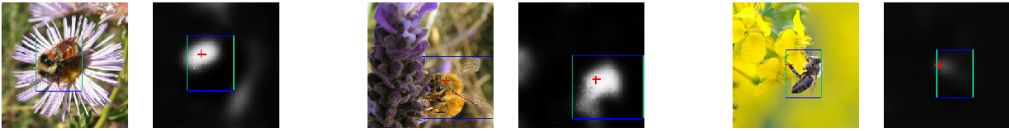


Figure 6.: Examples of how the ablation path saliency “points” in the bounding box of various images of bees. The bounding boxes are human defined in the dataset, the red crosses indicate the location of least-ablated pixel.

E for details on how we carried out the pointing game.

8. Conclusion

We demonstrated that the ablation path formalism provides a useful saliency method that combines ideas from previous methods within a robust mathematical framework. The ablation path method can stand in for each of these methods, and appears to be at least as reliable as they are.

This is a nontrivial result, because although the individual slices in a path arise from a similar optimisation problem as in [4], the optimisation of a whole path requires careful adjustment in order to fulfill the constraints (§ 3, Appendix Appendix C).

A practical advantage which is hard to quantify or demonstrate on paper, but evident when interactively browsing through a whole ablation path, is the added information: unlike each of the previous methods, an ablation path offers a whole sequence of changes to an input image and allows observing how each of them affects the network’s output. It thus offers a more thorough insight to the classification, while still ensuring the explanations form a consistent picture thanks to the monotonicity condition. Because each point in a path is associated with a concrete input to the network whose result can directly be inspected, we argue the method is *faithful* [18], whilst also being easy and intuitive to use and providing more information in addition to what previous methods also give.

We therefore suggest that our method is in many situations preferable to all previous ones we are aware of. The only clear disadvantage is that it is quite computationally expensive, but that is probably a minor concern in safety-critical applications and may actually be inextricable from the more powerful results: an optimised ablation path is informed by more real network evaluations than methods from [13], [4] or [3], and these evaluations are chosen with more purpose than in [8].

Remaining challenges for future work include a better notion of what behaviour should be considered adversarial vs. physical, convergence properties of the optimisation process (including the avoidance of vanishing-gradient issues / undersaturation), in connection with choice of parameters as well as choice of the baseline.

References

- [1] Adebayo, J., Gilmer, J., Muelly, M., Goodfellow, I., Hardt, M., Kim, B.: Sanity checks for saliency maps. In: Bengio, S., Wallach, H., Larochelle, H., Grauman, K., Cesa-Bianchi, N., Garnett, R. (eds.) *Advances in Neural Information Processing Systems* 31, pp. 9505–9515. Curran Associates, Inc. (2018), <http://papers.nips.cc/paper/8160-sanity-checks-for-saliency-maps.pdf>
- [2] Ancona, M., Ceolini, E., Öztireli, C., Gross, M.: Towards better understanding of gradient-based attribution methods for deep neural networks. *CoRR* (2017)
- [3] Fong, R., Mandela, P., Vedaldi, A.: Understanding deep networks via extremal perturbations and smooth masks. *ICCV* (2019), <https://arxiv.org/abs/1910.08485>
- [4] Fong, R., Vedaldi, A.: Interpretable explanations of black boxes by meaningful perturbation. *CoRR* (2017), <http://arxiv.org/abs/1704.03296v3>
- [5] Gildenblat, J.: Pytorch implementation of interpretable explanations of black boxes by meaningful perturbation. <https://github.com/jacobgil/pytorch-explain-black-box> (2017)
- [6] Kindermans, P.J., Hooker, S., Adebayo, J., Alber, M., Schütt, K.T., Dähne, S., Erhan, D., Kim, B.: The (un)reliability of saliency methods. *CoRR* (2017), <http://arxiv.org/abs/1711.00867v1>
- [7] Koh, P.W., Liang, P.: Understanding black-box predictions via influence functions. *CoRR* (2017), <http://arxiv.org/abs/1703.04730v2>
- [8] Petsiuk, V., Das, A., Saenko, K.: Rise: Randomized input sampling for explanation of black-box models. *CoRR* (2018)
- [9] Russakovsky, O., Deng, J., Su, H., Krause, J., Satheesh, S., Ma, S., Huang, Z., Karpathy, A., Khosla, A., Bernstein, M., Berg, A.C., Fei-Fei, L.: ImageNet Large Scale Visual Recognition Challenge. *International Journal of Computer Vision (IJCV)* **115**(3), 211–252 (2015). <https://doi.org/10.1007/s11263-015-0816-y>
- [10] Selvaraju, R.R., Cogswell, M., Das, A., Vedantam, R., Parikh, D., Batra, D.: Grad-cam: Visual explanations from deep networks via gradient-based localization. *CoRR* (2016), <http://arxiv.org/abs/1610.02391v4>
- [11] Simonyan, K., Vedaldi, A., Zisserman, A.: Deep inside convolutional networks: Visualising image classification models and saliency maps. *CoRR* (2013)
- [12] Sturmfels, P., Lundberg, S., Lee, S.I.: Visualizing the impact of feature attribution baselines. *Distill* (2020). <https://doi.org/10.23915/distill.00022>, <https://distill.pub/2020/attribution-baselines>

Appendix A. Canonical Time Reparametrisation

- [13] Sundararajan, M., Taly, A., Yan, Q.: Axiomatic attribution for deep networks. CoRR **abs/1703.01365** (2017), <http://arxiv.org/abs/1703.01365>
- [14] Szegedy, C., Ioffe, S., Vanhoucke, V., Alemi, A.: Inception-v4, inception-resnet and the impact of residual connections on learning (2016)
- [15] Szegedy, C., Zaremba, W., Sutskever, I., Bruna, J., Erhan, D., Goodfellow, I., Fergus, R.: Intriguing properties of neural networks (2014)
- [16] Tan, M., Le, Q.V.: Efficientnet: Rethinking model scaling for convolutional neural networks. CoRR **abs/1905.11946** (2019), <http://arxiv.org/abs/1905.11946>
- [17] Vedaldi, A.: Understanding deep networks via extremal perturbations and smooth masks. <https://github.com/facebookresearch/TorchRay> (2019)
- [18] Weller, A.: Transparency: Motivations and challenges. In: Samek, W., Montavon, G., Vedaldi, A., Hansen, L.K., Müller, K.R. (eds.) Explainable AI: interpreting, explaining and visualizing deep learning, vol. 11700, chap. 2. Springer Nature (2019)
- [19] Zhang, J., Bargal, S.A., Lin, Z., Brandt, J., Shen, X., Sclaroff, S.: Top-down neural attention by excitation backprop. International Journal of Computer Vision **126**(10), 1084–1102 (2017). <https://doi.org/10.1007/s11263-017-1059-x>

Appendix A. Canonical Time Reparametrisation

Proof of Lemma 3.2. The function $m: [0, 1] \rightarrow \mathbb{R}$ defined by $m(t) := \int_{\Omega} \varphi(t)$ is increasing and goes from zero to one (since we assume that $\int_{\Omega} 1 = 1$).

Note first that if $m(t_1) = m(t_2)$, then $\varphi(t_1) = \varphi(t_2)$ from the monotonicity property. Indeed, supposing for instance that $t_1 \leq t_2$, and defining the element $\theta := \varphi(t_2) - \varphi(t_1)$ we see that on the one hand $\int_{\Omega} \theta = 0$, on the other hand, $\theta \geq 0$, so $\theta = 0$ and thus $\varphi(t_1) = \varphi(t_2)$.

Now, define $M := m([0, 1]) = \{s \in [0, 1] \mid \exists t \in [0, 1] m(t) = s\}$. Pick $s \in [0, 1]$.

If $s \in M$ we define $\psi(s) := \varphi(t)$ where $m(t) = s$ (and this does not depend on which t fulfills $m(t) = s$ from what we said above). We remark that $\int_{\Omega} \psi(s) = \int_{\Omega} \varphi(t) = m(t) = s$.

Now suppose that $s \notin M$. Define $s_1 := \sup(M \cap [0, s])$ and $s_2 := \inf(M \cap [s, 1])$ (neither set are empty since $0 \in M$ and $1 \in M$). Since $s_1 \in M$ and $s_2 \in M$, there are $t_1 \in [0, 1]$ and $t_2 \in [0, 1]$ such that $m(t_1) = s_1$ and $m(t_2) = s_2$. Finally define $\psi(s) := \varphi(t_1) + (s - s_1) \frac{\varphi(t_2) - \varphi(t_1)}{s_2 - s_1}$. In this case, $\int_{\Omega} \psi(s) = m(t_1) + (s - s_1) \frac{m(t_2) - m(t_1)}{s_2 - s_1} = s$. The path ψ constructed this way is still monotone, and it has the constant speed property, so it is an ablation path. \square

Appendix B. \mathcal{L}^{∞} -optimal Monotonicity Projection

The algorithm proposed in Appendix Appendix C for optimising monotone paths uses updates that can locally introduce nonmonotonicity in the candidate $\hat{\varphi}_1$, so that it is

Appendix C. Path Optimisation Algorithm

needed to project back onto a monotone path φ_1 . The following routine³ performs such a projection in a way that is optimal in the sense of minimising the \mathcal{L}^∞ -distance⁴, i.e.,

$$\sup_t |\varphi_1(t, \mathbf{r}) - \hat{\varphi}_1(t, \mathbf{r})| \leq \sup_t |\vartheta(t, \mathbf{r}) - \hat{\varphi}_1(t, \mathbf{r})|$$

for all $\mathbf{r} \in \Omega$ and any other monotone path ϑ .

The algorithm works separately for each \mathbf{r} , i.e., we express it as operating simply on continuous functions $p : [0, 1] \rightarrow \mathbb{R}$. The final step effectively *flattens out*, in a minimal

Algorithm 1. Make a function $[0, 1] \rightarrow \mathbb{R}$ nondecreasing

```

 $\cup_i [l_i, r_i] \leftarrow \{ t \in [0, 1] \mid p'(t) \leq 0 \}$   $\triangleright$  Union of intervals where  $p$  decreases
for  $i$  do
   $m_i \leftarrow \frac{p(l_i) + p(r_i)}{2}$ 
   $l_i \leftarrow \max\{ t \in [r_{i-1}, l_i] \mid p(t) \leq m_i \}$ 
   $r_i \leftarrow \min\{ t \in [r_i, l_{i+1}] \mid p(t) \geq m_i \}$ 
end for
for  $i, j$  do
  if  $[l_i, r_i] \cap [l_j, r_j] \neq \emptyset$  then
    if  $m_j < m_i$ , merge the intervals and recompute  $m$  as the new center
  end if
end for
return  $t \mapsto \begin{cases} p(t) & \text{if } t \notin \cup_i [l_i, r_i] \\ m_i & \text{if } t \in [l_i, r_i] \end{cases}$ 

```

way, any region in which the function was decreasing.

In practice, this algorithm is executed not on continuous functions but on a PCM-discretised representation; this changes nothing about the algorithm except that instead as real numbers, l, r and t are represented by integral indices.

Appendix C. Path Optimisation Algorithm

As said in tsection § 5, our optimisation algorithm is essentially gradient descent of a path φ : it repeatedly seeks the direction within the space of all paths that (first ignoring the monotonicity constraint) would affect the largest increase to $P(\varphi)$ as per (2). As discussed before, this choice already requires a metric to obtain a vector-gradient from the covector-differential, which could be either the implicit ℓ^2 metric on the discretised representation (pixels), or a more physical kernel/filter-based metric. We conceptually use the latter, however for technical reasons do not immediately apply the corresponding

³It is easy to come up with other algorithms for monotonicising a (discretised) function. One could simply *sort the array*, but that is not optimal with respect to any of the usual function norms; or clip the derivatives to be nonnegative and then rescale the entire function, but that is not robust against noise perturbations.

⁴Note that the optimum is not necessarily unique.

Appendix C. Path Optimisation Algorithm

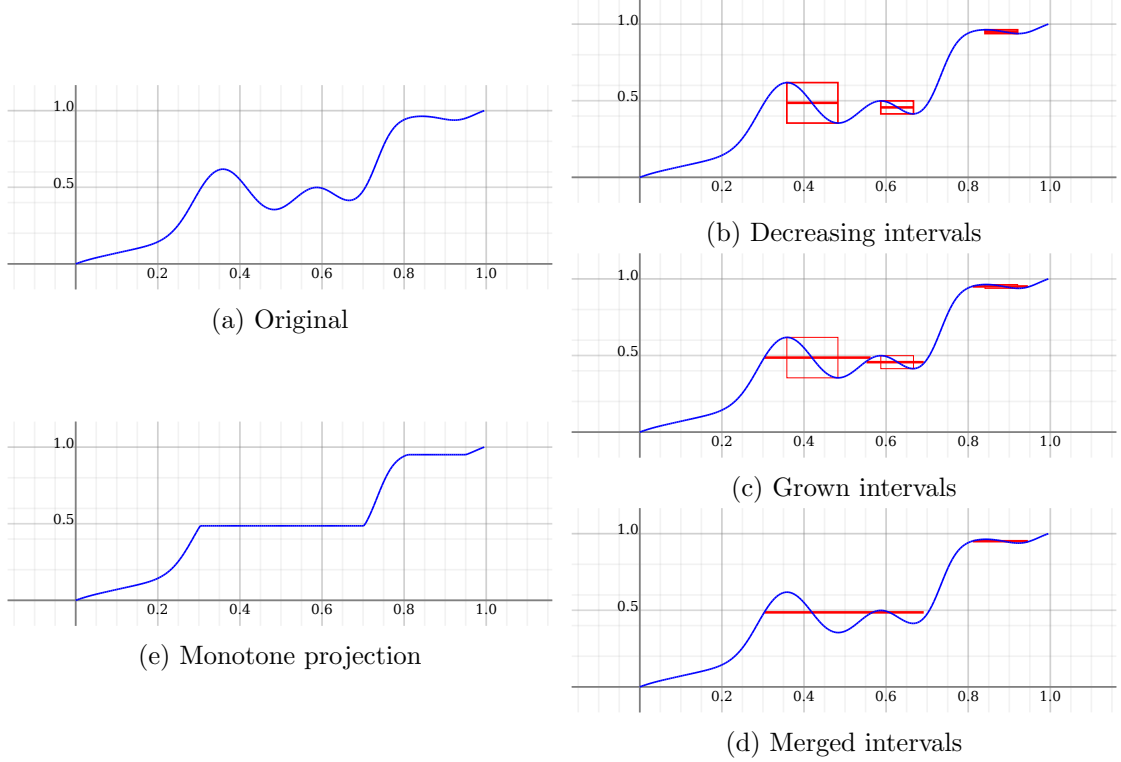


Figure 7.: Example view of the monotonicisation algorithm in practice. (a) contains decreasing intervals, which have been localised in (b). For each interval, the centerline is then extended to meet the original path non-decreasingly (c). In some cases, this will cause intervals overlapping; in this case merge them to a single interval and re-grow from the corresponding centerline (d). Finally, replace the path on the intervals with their centerline (e).

filter to the differential but rather to the *path*, which is not quite equivalent but does have the effect of avoiding noise from creeping into the state.

Unlike with the monotonicisation condition, the update can easily be made to preserve speed-constness by construction, by projecting for each t the gradient \mathbf{g} on the sub-tangent-space of zero change to $\int_{\Omega} \varphi(t)$, by subtracting the constant function times $\int_{\Omega} \mathbf{g}(t)$. Note this requires the measure of Ω to be normalised, or else considered at this point.

Then we apply these gradients time-wise as updates to the path, using a scalar product in the channel-space to obtain the best direction for φ itself (as opposed to the corresponding image composit $x_{\varphi,t}$).

Simply projecting the updates path then again to the set of legal (in the sense of Definition 3.1) ablation paths would presumably enough to converge towards a saturated path with high score, however in tests with artificial constant gradient we found out that this requires extremely many iterations, with the number apparently scaling with the

Algorithm 2. Projected Gradient Descent

```

1:  $\varphi \leftarrow ((t, \mathbf{r}) \mapsto t)$  ▷ Start with linear-interpolation path
2: while  $\varphi$  is not sufficiently saturated do
3:   for  $t$  in  $[0, 1]$  do
4:      $x_{\varphi, t} := (1 - \varphi(t)) x_0 + \varphi(t) x_1$ 
5:     compute  $F(x_{\varphi, t})$  with gradient  $\mathbf{g} := \nabla F(x_{\varphi, t})$ 
6:     let  $\hat{\mathbf{g}} := \mathbf{g} - \int_{\Omega} \mathbf{g}$  ▷ ensure  $\hat{\mathbf{g}}$  does not affect mass of  $\varphi(t)$ 
7:     update  $\varphi(t, \mathbf{r}) \leftarrow \varphi(t, \mathbf{r}) - \gamma \langle \hat{\mathbf{g}}(\mathbf{r}) \mid |x_1 - x_0\rangle$ , for  $\mathbf{r}$  in  $\Omega$  ▷  $\gamma$  is learning rate
8:     (optional) apply a filter to  $\varphi(t)$ 
9:   end for
10:  (optional) apply nonlinear gain to  $\varphi$ 
11:  for  $\mathbf{r}$  in  $\Omega$  do
12:    re-monotonise  $t \mapsto \varphi(t, \mathbf{r})$ , using Algorithm 1
13:  end for
14:  clamp  $\varphi(t, \mathbf{r})$  to  $[0, 1]$  everywhere
15:  re-parametrise  $\varphi$ , such that  $\int_{\Omega} \varphi(t) = t$  for all  $t$  (using Appendix Appendix A)
16: end while.
    
```

image dimension. The problem here is that saturating updates tend to be undone again by the speed-normalising reparametrisation, except for the most affected pixel. (Just increasing the learning rate does not help with this.) If the gradients come from a deep CNN and for every pixel the monotonicity needs to be restored, such many iterations would be prohibitly computation-intensive.

Fortunately we can dramatically speed up the convergence by artificially encouraging saturation. We tweak the ablation path φ pointwise with a sigmoidal function that brings values lower than $\frac{1}{2}$ slightly closer to 0, and values greater than $\frac{1}{2}$ slightly closer to 1. To this end, we use a perturbation of the identity function defined by $x \mapsto x + \epsilon(x)$, and apply it pointwise to the path:

$$\varphi(\mathbf{r}, t) \leftarrow \varphi(\mathbf{r}, t) + \epsilon(\varphi(\mathbf{r}, t))$$

The perturbation function $\epsilon: [0, 1] \rightarrow \mathbb{R}$ has the property that $x + \epsilon(x)$ maps $[0, 1]$ into itself. The function ϵ we use is plotted on Figure 8. Although this perturbation seems small, the examples in § 6 now only require 20-40 iterations.

As to the motivation behind the transformation $\varphi \rightarrow \varphi + \epsilon(\varphi)$, notice first that fully saturated masks – i.e., those that choose for every pixel are either zero or one, selecting exactly the value of either the current target or the baseline – are fixpoints of the function $x \mapsto x + \epsilon(x)$ since $\epsilon(0) = \epsilon(1) = 0$. So if such a mask is the optimum in the algorithm without artificial saturation (while there is no guarantee for this in general, this seems fairly frequent in practice), then it will also be an optimum of the algorithm with artificial saturation.

What is more, the dynamical system $x \mapsto x + \epsilon(x)$ quickly converges to zero or one, which efficiently encourages saturation, without sacrificing precision, as the function ϵ we chose is quite small.

Appendix D. Baseline choice

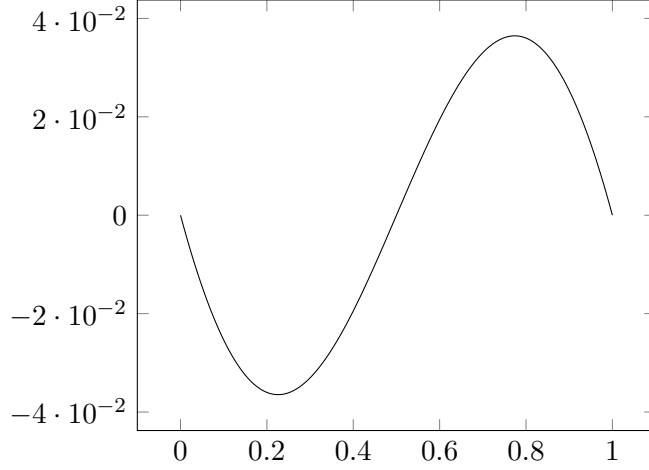


Figure 8.: Function $\epsilon: [0, 1] \rightarrow \mathbb{R}$. Note that $|\epsilon(x)| \leq 5 \times 10^{-2}$. The formula is $\epsilon(x) := \tanh(2\zeta(x - 1/2))/2 \tanh(\zeta) + 1/2 - x$, with $\zeta = 0.8$.

Conversely, and unlike high learning rate, the saturation function is by construction monotone, symmetric and keeps the signal within the allowed bounds, so it avoids violating the ablation path constraints. The problem with high learning rates is that the algorithm gets caught in a sequence of alternating strong constraint-violating updates followed by a projection step that largely undoes the previous update.

Appendix D. Baseline choice

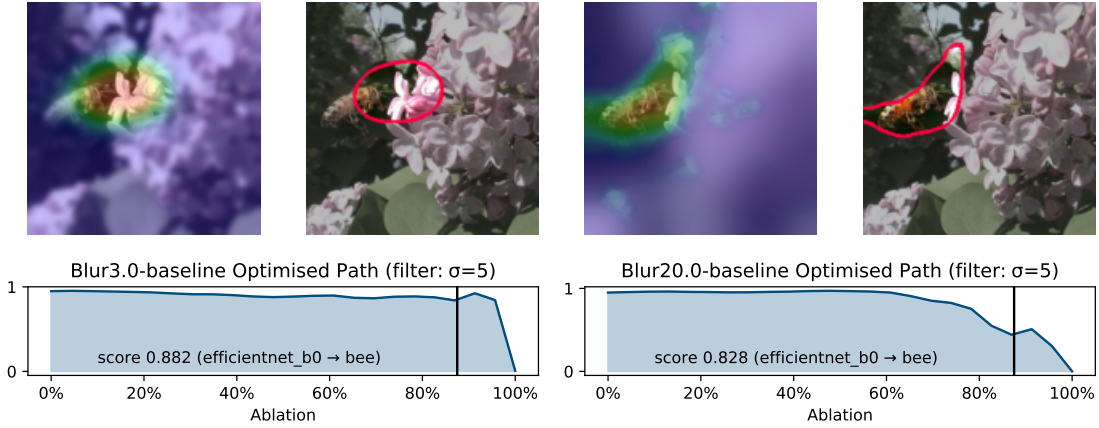


Figure 9.: The example from Figure 3 evaluated different different baselines, still gaussian blurred versions of the target image but with different sizes of the blur filter.

The baseline image is prominently present in the input for much of the ablation path,

and it is therefore evident that it will have a significant impact on the saliency. In line with previous work, we opted for a blurred baseline for the examples in the main paper, but even then there is still considerable freedom in the choice of blurring filter. Figure 9 shows two examples, where the result is not fundamentally, but still notably different.

Appendix E. Evaluation with Pointing Game

The Pointing Game, the results of which we show in §7, is a way to verify that the saliency method points at a region that a human would consider relevant to the classification. It is often the region of an image that contains the physical object which is being classified.

Our method has an advantage over other ones as it yields not only a single spatial map as the saliency but a whole path of masks. However, it does not directly give a single saliency map comparable to what other methods yield. Here is how we choose one point in the image from an ablation path. First, we seed the threshold mask; cf. also §6. By default, for the pointing game we chose the time at which the probability has dropped by 20 %, that is the smallest time t such that $F(t) \leq 0.8$. When there is no such time, we pick the one for which F takes the maximum value on the path. Now that the time is chosen, we pick the point in the mask which have the smallest value. Note that, even though this selection may be unstable (since many points are close to the minimum value, as the mask is typically saturated), it usually does not matter since the whole region selected by the mask is salient.

The classifier in this experiment was an EfficientNet [16] pre-trained on ImageNet, the test data set 360 images from three synsets out of ImageNet.

As a comparison, we evaluated the pointing game with the same network and inputs also through the closely related Meaningful Perturbations method [4]. We used a third-party PyTorch implementation [5]. Note that this implementation uses a slightly simplified method of removing information for performance, and that we did not change any of the hyperparameters of the method, so it is very likely that these results are not optimal. We also note that [4] themselves include results for the pointing game on different data, with better scores.

Nevertheless, the point was to show that our method works reasonably well, and this may be due to the use of ablation paths: that increasing family of mask probably gives some stability to the saliency method, which improves the scores.

Appendix F. Random ablation paths

In this section, following an idea of [12], we compare our method to random ablation-paths like the example shown in Figure 4. Figure 10 shows that this typical behaviour. In the unsmoothed case, the scores are almost compactly clustered in the middle, i.e., paths consisting of random single-pixel transitions rarely have exceptional scores. If the random paths are spatially smoothed, outliers become more likely (the paths could by coincidence mask out a whole particularly relevant region), but the scores are still really unlikely to reach 0.9, something our optimisation approach routinely attains.

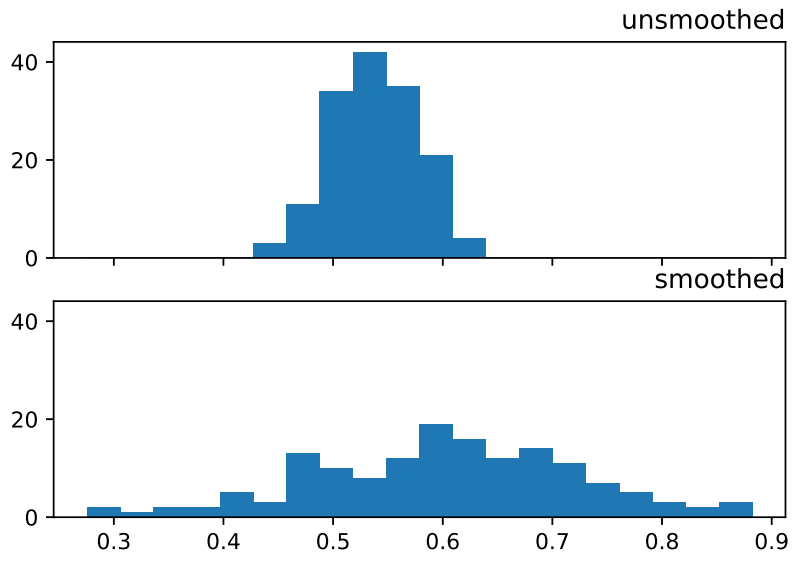


Figure 10.: Histograms of the scores of ablating an image obtained as explained in § 4.2 (an image of a gold finch, against its blurred baseline) along random paths.